

## Structure Basis of Ca<sub>v</sub>1.1 Modulation by Dihydropyridine Compounds

### Authors

Shuai Gao, Nieng Yan\*

### Affiliations

Department of Molecular Biology, Princeton University, Princeton, NJ 08544, USA

\*To whom correspondence should be addressed: N. Yan (nyan@princeton.edu)

### Abstract

1,4-Dihydropyridines (DHP), the most commonly used antihypertensives, function by inhibiting the L-type voltage-gated Ca<sup>2+</sup> (Ca<sub>v</sub>) channels. DHP compounds exhibit chirality-specific antagonistic or agonistic effects. Recent structural elucidation of rabbit Ca<sub>v</sub>1.1 bound to an achiral drug nifedipine reveals the general binding mode for DHP drugs, but the molecular basis for chiral specificity remains elusive. Here, we report five cryo-EM structures of nanodisc-embedded Ca<sub>v</sub>1.1 in the presence of the bestselling drug amlodipine, a DHP antagonist (R)-(+)-Bay K8644, and a titration of its agonistic enantiomer (S)-(-)-Bay K8644 at resolutions of 2.9-3.4 Å. The amlodipine-bound structure reveals the molecular basis for the high efficacy of the drug. All structures with the addition of the Bay K8644 enantiomers exhibit similar inactivated conformations, suggesting that the agonistic effect of (S)-(-)-Bay K8644 might be transient. The similarity of these structures to that obtained in detergent micelles alleviates the concerns about potential structural perturbation by detergents.

## Introduction

Voltage-gated  $\text{Ca}^{2+}$  ( $\text{Ca}_v$ ) channels (VGCC) are responsible for a broad spectrum of physiological events, including muscle contraction, secretion, and synaptic signal transduction (1, 2). In mammals, 10 subtypes of  $\text{Ca}_v$  channels are classified to three subfamilies:  $\text{Ca}_v1$  ( $\text{Ca}_v1.1$ - $\text{Ca}_v1.4$ ),  $\text{Ca}_v2$  ( $\text{Ca}_v2.1$ - $\text{Ca}_v2.3$ ), and  $\text{Ca}_v3$  ( $\text{Ca}_v3.1$ - $\text{Ca}_v3.3$ ).  $\text{Ca}_v1$  channels, also known as the L-type VGCCs or dihydropyridine (DHP) receptors (DHPRs), are composed of a core  $\alpha1$  subunit and three auxiliary subunits,  $\alpha2\delta$ ,  $\beta$ , and  $\gamma$  (3, 4). The  $\alpha1$  subunit is a single polypeptide of ~2000 amino acids, folding into four homologous repeats I-IV. Each repeat contains six transmembrane segments (S1-S6) that form two functional entities: segments S1-S4 in each repeat constitute the peripheral voltage sensing domains (VSDs), and the S5-S6 segments from all four repeats, together with the intervening pore helices P1 and P2, enclose the central ion-permeating pore domain (PD). The short fragments between P1 and P2 from the four repeats serve as the molecular sieve, known as the selectivity filter (SF), which discriminates calcium from other ions (1-4).

Dysfunctional  $\text{Ca}_v$  channels are associated with various pathophysiological conditions ranging from cardiovascular disorders to psychiatric and neurological syndromes, such as cardiac arrhythmias, seizures, epilepsy, autism and Parkinson's disease (1-4). Antagonists of DHPRs have demonstrated excellent efficacy in clinical practice for the treatment of specific conditions, including hypertension, cardiac ischemia, pain and tremor (5).

Among the  $\text{Ca}_v$  antagonists, DHP compounds are the most widely prescribed drugs, which, exemplified by amlodipine and nifedipine, have been the world's bestsellers for decades

(6, 7). Benzothiazepines (BTZ) and phenylalkylamines (PAA) represent the other two major classes of DHPR-targeting drugs (6, 8, 9). While BTZ and PAA compounds directly block ion conduction by traversing the central cavity of the pore domain, DHP antagonists bind to the fenestration, which is the portal on the side wall of the PD, on the interface of repeats III and IV for allosteric modulation (9).

While DHP drugs act as antagonists, some DHP compounds exhibit agonistic effects on DHPRs. Even more intriguingly, the mode of action (MOA) of some DHP compounds is stereoselective; enantiomers of these DHP ligands possess opposite pharmacological profiles (10). For instance, whereas compound (*S*)-(-)-Bay K8644 is a potent agonist for DHPRs, its enantiomer, (*R*)-(+)-Bay K 8644 displays antagonistic activity (Fig. 1A) (11, 12). It is also noted that (*S*)-(-)-Bay K8644 produces a biphasic dose-response effect, whereby the agonist is turned to an antagonist when applied at high concentrations (13, 14). The biphasic property is also observed for modulators of other membrane proteins, such as dopamine D-2 and cannabinoid receptors, for which the usage dose should be finely regulated to achieve the desired efficacy (15, 16).

An in-depth understanding of the MOA of these modulators requires high-resolution structures. Due to the advances of the resolution revolution of single-particle cryogenic electron microscopy (cryo-EM), we were able to resolve the structures of the rabbit Ca<sub>v</sub>1.1 (rCa<sub>v</sub>1.1) channel complex and human Ca<sub>v</sub>3.1 alone and in the presence of various small molecule ligands (17-20). Specifically, the atomic structures of rCa<sub>v</sub>1.1 bound to representative DHP, BTZ, and PAA drugs, nifedipine, diltiazem, and verapamil, respectively, have elucidated the molecular details of the drugs' action (19).

Notwithstanding these exciting structural advances, there are a number of outstanding questions. First, all the reported structures of eukaryotic Ca<sub>v</sub> channels and the closely related Na<sub>v</sub> channels are of proteins purified in detergent micelles. It is unclear whether the detergents have altered local structures of these highly dynamic channels. As such, structural elucidation in a more physiologically relevant environment, such as in nanodiscs, is required. Second, in the structure of Ca<sub>v</sub>1.1 complexed with the agonist (*S*)-(-)-Bay K8644, the overall structure conforms to what is expected to be an inactivated state (19). (*S*)-(-)-Bay K8644 was applied at 100 μM, a dose at which the compound may function as an antagonist. It remains to be tested whether the agonist at lower concentration can help lock the channel in an activated state. Last but not least, both DHP compounds, (*S*)-(-)-Bay K8644 and nifedipine, have relatively small chemical groups, but it has yet to be seen how the bulkier groups of some DHP drugs, such as levamlodipine (amlodipine for short hereafter), are coordinated by DHPR.

To address these remaining questions, we sought to resolve the structures of rabbit Ca<sub>v</sub>1.1 reconstituted in nanodiscs with addition of representative DHPR compounds. Here we report high-resolution cryo-EM structures of nanodisc-embedded Ca<sub>v</sub>1.1 bound to the antagonists amlodipine and (*R*)-(+)-Bay K 8644, and a titration of (*S*)-(-)-Bay K8644 (Fig. 1A). These structures together provide advanced knowledge on the modulation of DHPRs by DHP compounds. For simplicity, we will refer to the enantiomers of Bay K 8644 as RBK and SBK hereafter.

## Results

## **Structures of Ca<sub>v</sub>1.1 in lipid nanodiscs are nearly identical to those in detergent micelles**

Following our published protocols (17, 21), Ca<sub>v</sub>1.1 isolated from the skeletal muscle of New Zealand white rabbits, rCa<sub>v</sub>1.1, was purified and reconstituted into nanodiscs with the membrane scaffold protein 2N2 (MSP2N2) and POPC (Fig. 1B, S1). Please refer to Methods for details of the protein purification and nanodisc reconstitution. The mono-dispersed peak fractions of rCa<sub>v</sub>1.1 nanodiscs from size-exclusion chromatography were pooled and incubated with the target molecules before cryo-sample preparation. Amlodipine and RBK were applied at 100 μM, and SBK was added at final concentrations of 1 μM, 10 μM, and 100 μM, in the hope of capturing different channel states.

The cryo-grids were made following a standard protocol and electron micrographs were collected on Titan Krios G3 cryo-electron microscope equipped with the spherical aberration (Cs) image corrector and GIF quantum electron energy filter. The workflow for data processing is described in SI (Fig. S2, S3). The overall resolutions of the channel complexes were determined at 2.9 Å with amlodipine, 3.2 Å with RBK, and 3.4 Å, 3.4 Å, and 3.0 Å with SBK at 1 μM, 10 μM, and 100 μM, respectively. For simplicity, we will refer to these five structures as rCa<sub>v</sub>1.1-100A (with 100 μM amlodipine), 100R (with 100 μM RBK), and 1S/10S/100S (with SBK applied at three different concentrations). Our published structure of digitonin-embedded rCa<sub>v</sub>1.1 in the presence of 200 μM nifedipine, used as structural reference several times in this manuscript, will be referred to as rCa<sub>v</sub>1.1-200N (PDB code: 6JP5) (19). The excellent map quality and high local resolutions allow for accurate assignment of the DHP ligands (Fig. 1C, S4).

The overall structures of rCa<sub>v</sub>1.1 in complex with the DHP antagonists, amlodipine and RBK, in nanodiscs are nearly identical to rCa<sub>v</sub>1.1-200N. The structures of the  $\alpha$ 1 subunit in rCa<sub>v</sub>1.1-100A and rCa<sub>v</sub>1.1-100R can be superimposed to that in rCa<sub>v</sub>1.1-200N with root-mean-square deviation (RMSD) values both of 0.52 Å over 1115 C $\alpha$  atoms (Fig. 2A, B). This observation in part supports that the previous structure-function relationship studies of rCa<sub>v</sub>1.1 obtained in a detergent surrounding can be repeated in lipid membrane environment.

The DHP agonist, SBK, was titrated into the purified rCa<sub>v</sub>1.1 embedded in nanodiscs at the final concentration of 1  $\mu$ M, 10  $\mu$ M, and 100  $\mu$ M, respectively, immediately before cryo-sample preparation. In all three nanodisc-surrounded reconstructions, the intracellular gate is closed and the four VSDs exhibit depolarized conformations, characteristic of the same putative inactivated state as our previously reported SBK-bound rCa<sub>v</sub>1.1 in digitonin (PDB code: 6JP8) (19). The overall structures of rCa<sub>v</sub>1.1-100S in nanodiscs and in detergents can be well aligned with a root-mean-square deviation (RMSD) values of 0.55 Å over 1115 C $\alpha$  atoms for  $\alpha$ 1 subunit (Fig. 2C). This observation partially alleviates the concern with potential interference of the conformations of Ca<sub>v</sub>1.1, and probably all other single-chain Ca<sub>v</sub> and Na<sub>v</sub> channels whose structures have been resolved, by detergents.

### **Nearly identical state of rCa<sub>v</sub>1.1 in complex with a titration of SBK**

As aforementioned, the DHP agonist, SBK, was added into nanodisc-embedded rCa<sub>v</sub>1.1 at a concentration gradient with the aim to capture different channel states. The EM densities corresponding to SBK are only observed in rCa<sub>v</sub>1.1-10S/100S, leaving the rCa<sub>v</sub>1.1-1S as an apo reconstruction (Fig. 3A). SBK is nestled into the same fenestration site enclosed by the pore-

forming elements of repeats III and IV, surrounded by residues on the segments P1<sub>III</sub>, S5<sub>III</sub>, S6<sub>III</sub> and S6<sub>IV</sub> (Fig. 3B). Because the detailed coordination of SBK is identical to our reported one (19), it will not be elaborated here.

The EM density for SBK in rCa<sub>v</sub>1.1-10S is worse than that in rCa<sub>v</sub>1.1-100S, implying less stable coordination. A close examination shows a slight difference in the densities for the bound SBK in rCa<sub>v</sub>1.1-10S and -100S, especially those for the C3-ester group. Structural models were built for SBK in rCa<sub>v</sub>1.1-10S, which displaces slightly from that in rCa<sub>v</sub>1.1-100S. In particular, the C3-ester group appears to undergo a rotation (Fig. 3C). This minor difference may not change its function as an antagonist to rCa<sub>v</sub>1.1 in this particular conformation. Nevertheless, this observation is consistent with our previous analysis on the meta-stable association between rCa<sub>v</sub>1.1 and SBK.

Due to the lack of ligand density, rCa<sub>v</sub>1.1-1S may represent the state of an apo-structure, hence providing a good control to trace the conformational changes of rCa<sub>v</sub>1.1 upon SBK binding. The only difference occurs in Gln939 on S5<sub>III</sub> (Fig. 3D). Upon SBK entry, Gln939 rotates toward Tyr1048 of S6<sub>III</sub> and mediates the essential H-bond network between the ester group of SBK and Tyr1048. It was reported that single point mutations corresponding to Y1048F and Y1048A resulted in reduced affinity with DHP by ~10- and ~1,000-fold, respectively (22). Our structural comparison suggests that Tyr1048 may be required for DHP association through facilitating the shift of Gln939. Rotation of Gln939 driven by Tyr1048 paves the path for the entry of DHP ligands, followed by the stabilization from the hydrophobic and H-bond interactions with the surrounding residues in the fenestration site.

It is noted that a density corresponding to a phospholipid was well-resolved outside the fenestration (Figure 3E, Fig. S5A). One aliphatic tail of the lipid blocks the fenestration and interacts directly with SBK. This arrangement may prevent the ligand from exiting the binding site. The role of phospholipid in ligand binding to membrane proteins has rarely been discussed. Our structural finding provides a clue to understanding the sophisticated ligand binding within membrane.

### Comparison for DHP enantiomers

SBK and RBK are a pair of DHP enantiomers with a chiral center on the C4 atom of the dihydropyridine ring. In rCa<sub>v</sub>1.1-100R, RBK is positioned in the same fenestration site as that for SBK in rCa<sub>v</sub>1.1-10S/100S (Fig. 4A). Compared to SBK in rCa<sub>v</sub>1.1-100S, the CF<sub>3</sub>-substituted phenyl ring of RBK projects into the hydrophobic pocket formed by Thr935, Val932, and Phe1060, while the dihydropyridine flips over ~180 degree (Fig. 4B). In this way, the nitro group of RBK is H-bonded to Tyr1048/Gln939 and Thr935, similar to the role of C3-ester in SBK.

On the other hand, the C3-ester of RBK is situated into a hydrophobic cavity surrounded by Met1366, Val932, and Phe1060 (Fig. 4C). The binding pose of RBK can be superimposed to that for nifedipine (PDB:5JP5), suggesting a conserved conformation for DHP antagonists (Fig. 4D). Besides, the cryo-EM coordination of RBK in nanodisc-embedded rCa<sub>v</sub>1.1 is consistent with our previous docking result using the aforementioned nifedipine-bound structure as template (19).



## Coordination of amlodipine

Amlodipine is the most potent DHP antagonist that displays a pH-dependent efficacy (23). As expected, it is also nestled in the III-IV fenestration of the PD. Despite the larger size, coordination for the backbone of amlodipine is nearly identical with that for nifedipine, involving residues Ser1011, Tyr1048, Gln939, Thr935, and Met1366 (Fig. 5A, B).

The bulky substituent in amlodipine, the ethanolamine group, points to the central cavity of the PD and is H-bonded to the carbonyl group of S1011 (Fig. 5A, B). Except for this group, the interactions between amlodipine and the surrounding residues are highly conserved similar to other antagonists in rCa<sub>v</sub>1.1, including three pairs of H-bonds, two between C3-ester and Tyr1048/Gln939/Thr935, and one between N1 atom and S1011.

Amlodipine displays longer duration time of action than nifedipine, allowing a once-a-day dosage regimen in human (24). Based on our structure, the improved pharmacological profile of amlodipine may come from the ethanolamine group. The introduction of ethanolamine group not only increases the aqueous solubility, but also enhances the binding affinity of amlodipine by the formation of an additional H-bond with the conserved residue in Ca<sub>v</sub>1 that corresponds to Ser1011 in rCa<sub>v</sub>1.1 (Fig. 5C).

## Potential role of lipids in DHP ligand coordination

In addition to the compound and surrounding residues, EM densities corresponding to lipids were resolved in the central cavity of DHP-bound rCa<sub>v</sub>1.1. It is noteworthy that such densities were also observed in the digitonin solubilized conditions for both ligand-free and antagonists-

bound rCa<sub>v</sub>1.1 reconstructions. Although the resolution is insufficient to identify specific lipids, the contour allowed for putative docking of the lipid 1-palmitoyl-2-oleoyl-sn-glycero-3-phosphoethanolamine (16:0-18:1 PE), a major lipid component of eukaryotic cell membrane (18).

Given the proximity to the molecules, the lipid appears to directly contribute to the binding of amlodipine. Specially, in rCa<sub>v</sub>1.1-100A, the phosphate group of the lipid approaches the fenestration site and interacts with the ethanolamine substituent of amlodipine (Fig. 5C,D, Fig. S5B). Although the exact identity of this specific lipid cannot be identified due to technical limitations, the phosphate is the common functional group in all phospholipids, which indicates that the phosphate group of the native lipid may provide further stabilization for amlodipine (Fig. 5D).

## Discussion

rCa<sub>v</sub>1.1 was the first single-chain VGIC (voltage-gated ion channels) whose structure was determined (17, 18). We have been employing it as a prototype for cryo-EM analysis of VGIC members. Before this study, all the structures of rCa<sub>v</sub>1.1, as well as the closely related human Ca<sub>v</sub>3.1 and multiple eukaryotic Na<sub>v</sub> channels, were solved as proteins embedded in detergents (25-30). We have had some concerns with potential structural perturbation of these highly dynamic molecular machines by detergents. The structural similarity of rCa<sub>v</sub>1.1 in nanodiscs and in detergent micelles, which was also observed in our recently published NaChBac (31), alleviates this concern and consolidates the structural findings obtained from the detergent-embedded channels. More satisfyingly, the coordination of the backbones of all resolved DHP

antagonists, nifedipine (19), amlodipine, and RBK, is conserved regardless of the surrounding milieu of detergents or nanodiscs.

The high resolutions of rCa<sub>v</sub>1.1 in complex with different DHP compounds allowed for detailed analyses of ligand binding, providing the basis to understand the distinct efficacy of the drugs and functional groups of the channel. The direct participation of a phospholipid in the coordination of amlodipine is intriguing in that it is unclear whether a phospholipid can enter the central cavity in the intact membrane. Although our structure was obtained in nanodiscs, the native membrane was disrupted during protein extraction and purification. Therefore, this remains to be an enigma that awaits further investigation. Multiple biophysical and computational approaches are needed to dissect the mechanism and the function of the transverse lipids in the physiology and pharmacology of VGIC channels.

We had aimed to utilize the well-characterized agonist SBK to capture the channel in an activated state. Despite our attempt to apply SBK at different doses and in different environments, the channel remains in the same inactivated state. Notably, when applied at 1  $\mu$ M, the density corresponding to SBK was gone. This observation supports our previous analysis that the SBK is not favored by the inactivated conformation. Therefore, a high concentration is required to compensate for the penalty (19). This set of structural analyses suggest that an agonist, whose action is to prolong the opening duration of the channel(32-34), is insufficient to lock the channel in an active conformation. Because it is impractical to conveniently introduce point mutations to the endogenous channels, it may require the invention of new methods to capture voltage-gated ion channels in distinct functional states.

Despite the remaining questions, our structural analyses reported here and previously (19) provide a more comprehensive understanding of the MOA of DHP drugs. This updated knowledge will facilitate drug discovery targeting other Ca<sub>v</sub> channels and additional VGICs in general.

## Figure Legends

**Fig. 1 | Cryo-EM analysis of Ca<sub>v</sub>1.1 in complex with amlodipine, RBK, and SBK in nanodiscs.** (A) Chemical structures of (S)-(-)-Bay K8644, (R)-(+)-Bay K8644, and levamlodipine. (B) Final purification step for rCa<sub>v</sub>1.1 in MSP2N2-surrounded nanodiscs. Shown here is a representative size-exclusion chromatogram (SEC) and Coomassie blue-stained SDS-PAGE. (C) Local resolution maps and densities for the bound ligands. The densities in the lower row, shown as blue mesh, are contoured at 3  $\sigma$  and prepared in PyMol.

**Fig. 2 | Nearly identical conformations of DHP antagonists-bound rCa<sub>v</sub>1.1 in detergents and in nanodiscs.** (A) Overall structure of the amlodipine-bound rCa<sub>v</sub>1.1 complex (rCa<sub>v</sub>1.1-100A) at 2.9 Å resolution. The overall structure of the channel complex is shown for different subunits. The  $\beta$ 1 subunit is omitted throughout the manuscript because of its poor resolution. Amlodipine is shown as orange spheres and the bound lipids are shown as grey sticks. (B) The overall structures of rCa<sub>v</sub>1.1 in complex with amlodipine (pink) and RBK (cyan) in nanodiscs and nifedipine (grey) in digitonin are nearly identical. (C) Structures of rCa<sub>v</sub>1.1 in complex with 100  $\mu$ M SBK in nanodisc (green) and in digitonin (blue) are nearly identical.

**Fig. 3 | The conformation of nanodisc-embedded rCa<sub>v</sub>1.1 remains nearly unchanged with**

**SBK applied at different conformations.** (A) Structural comparison of rCa<sub>v</sub>1.1 in complex with 100  $\mu$ M SBK (green), 10  $\mu$ M SBK (wheat), and 1  $\mu$ M SBK (cyan) in nanodisc. Despite the different concentrations of SBK applied, the overall structure remains nearly unchanged. (B) There is no density of SBK in the EM reconstruction when applied at 1  $\mu$ M. The densities for SBK and its binding site in rCa<sub>v</sub>1.1-100S/10S/1S are shown. The maps, shown as blue mesh, are contoured at 7 $\sigma$  and prepared in PyMol. (C) Slight displacement of SBK between rCa<sub>v</sub>1.1-100S (black) and 10S (brown). The electrostatic surface potential of rCa<sub>v</sub>1.1-100S was calculated in PyMol. (D) Gln939 on S5<sub>III</sub> of rCa<sub>v</sub>1.1-100S (green) shifts to Tyr1048 compared to rCa<sub>v</sub>1.1-1S (cyan). Such local conformational shift is important for accommodating the ligand. (E) A lipid may contribute to SBK coordination. SBK and lipid are shown as sticks and colored black and gray, respectively. SBK is coordinated by both polar and hydrophobic residues. One hydrophobic tail of a phospholipid blocks the III-IV fenestration, strengthening SBK binding. Potential hydrogen bonds are shown as dashed lines.

**Fig. 4 | Coordination of the antagonistic RBK by rCa<sub>v</sub>1.1.** (A) The densities for the RBK

binding site in rCa<sub>v</sub>1.1-100R. RBK is shown as yellow sticks. The densities, shown as blue mesh, are contoured at 7  $\sigma$  and prepared in PyMol. (B) Overlapping binding site for RBK and SBK. The structures of rCa<sub>v</sub>1.1-100R (blue) and -100S (green) are superimposed. RBK and SBK are colored yellow and black, respectively. (C) Coordination of RBK. Potential hydrogen bonds are shown as dashed lines. (D) Overlapping binding site for RBK and nifedipine. The structure rCa<sub>v</sub>1.1-100R (yellow) and nifedipine (gray) are superimposed. The NO<sub>2</sub> group in RBK, which is

positioned adjacent to S5<sub>III</sub> segment, is highlighted with black circle. The C3-ester groups of RBK and nifedipine are highlighted with pink shadow.

**Fig. 5 | Specific interactions between rCa<sub>v</sub>1.1 and Amlodipine.** (A) The density for amlodipine binding sites in rCa<sub>v</sub>1.1-100A. Amlodipine is shown as purple sticks. The densities, shown as blue mesh, are contoured at 7 $\sigma$  and prepared in PyMol. (B) Overlapping binding site for amlodipine and nifedipine. The structure rCa<sub>v</sub>1.1-100A (pink) and nifedipine (gray) are superimposed. The ethanolamine group in amlodipine is highlighted with orange shadow. (C) Coordination of amlodipine at the III-IV fenestration of rCa<sub>v</sub>1.1. (D) A transverse lipid in the central cavity contributes to amlodipine binding. The phosphate group (orange colored) of the lipid (grey for the backbone) and Ser1011 coordinate the ethanolamine group of amlodipine from two opposite directions. Please refer to figure S5B for the density of the lipid.

## Materials and Methods

### Expression and purification of GST- $\beta$ 1a

The GST-fused  $\beta$ 1a protein was expressed and purified as previously reported (17). Briefly, overexpression of GST-  $\beta$ 1a was carried out using *Escherichia coli* BL21 (DE3) (Novagen) transformed with plasmid containing the cDNA inserted into pGEX-4T-2 vector. The resulting *E.coli* was cultured at 37 °C in LB medium with 100 mg/mL ampicillin (AMRESCO) to OD<sub>600</sub> of 1.2. Then the culture temperature was cooled down to 18 °C, and 0.2 mM isopropyl- $\beta$ -D-thiogalactoside was added for protein expression induction. After 12 h culture, the cells were collected and resuspended with lysis buffer containing 25 mM Tris-HCl, pH 8.0 and 150 mM NaCl. Sonication was adopted for cell disruption. After centrifugation at 27,000 g for 1 h, the

supernatant was collected and applied to Glutathione Sepharose 4B resin (GS4B, GE Healthcare) and washed with lysis buffer. The protein was eluted with elution buffer containing 50 mM Tris-HCl, pH 8.0, 50 mM NaCl and 10 mM glutathione. The ion-exchange chromatography was performed for further protein purification with an anion-exchange column (Source 15Q, GE Healthcare). Then peak fractions were collected and stored at -80 °C before using.

### **Isolation of skeletal muscle membrane from New Zealand white rabbits**

This step was well described previously (17). Fresh skeletal muscle was isolated from rabbit legs and back, and then was homogenized in buffer containing 0.3 M sucrose, 10 mM MOPS-Na, pH 7.4, 0.5 mM EDTA and protease inhibitors mixture including 2 mM phenylmethylsulphonyl fluoride (PMSF), 1.3 mg/mL aprotinin, 0.7 mg/mL pepstatin and 5 mg/mL leupeptin. Two steps centrifugation were performed. The homogenates were first centrifuged at 5,000 g for 5 min, following by a second centrifugation at 200,000 g for 1 h of the supernatant. The pellet was collected and stored at -80 °C before using.

### **Protein preparation**

The Ca<sub>v</sub>1.1 complex from rabbit skeletal muscle was purified as described previously. In brief, the collected skeletal muscle was solubilized in buffer containing 20 mM MOPS-Na, pH 7.4, 500 mM NaCl, 0.5 mM CaCl<sub>2</sub>, 1% (w/v) GDN (Anatrace), 2 mM PMSF, 3.9 mg/mL aprotinin, 2.1 mg/mL pepstatin, 15 mg/mL leupeptin and excessive GST-β1a at 4 °C for 2 h. The mixture was then ultra-centrifuged at 200,000 g for 30 min, and the supernatant was applied to GS4B resin. The protein-loaded resin was washed with buffer containing 20 mM MOPS-Na, pH 7.4, 500 mM NaCl, 0.5 mM CaCl<sub>2</sub>, 0.01% GDN and protease inhibitors. Protein elution was performed with buffer containing 100 mM Tris-HCl, pH 8.0, 200 mM NaCl, 0.5 mM CaCl<sub>2</sub>, 15 mM reduced

glutathione, 0.01% GDN, and protease inhibitors. The fused GST was removed with addition of HRV 3C protease, followed by the size-exclusion chromatography (Superose 6 10/300 GL, GE Healthcare) in buffer containing 20 mM MOPS-Na, pH 7.4, 200 mM NaCl, 0.5 mM CaCl<sub>2</sub>, 0.01% GDN and protease inhibitors.

### **Nanodisc reconstitution**

Lipid 1-palmitoyl-2-oleoyl-glycero-3-phosphocholine (POPC, Avanti) in chloroform was dried under a nitrogen stream and resuspended in reconstitution buffer containing 25 mM Tris-HCl, pH 8.0, 150 mM NaCl, and 0.7% DDM. Approximately 250 µg purified protein was mixed with 1 mg MSP2N2 and 750 µg lipid. The mixture was incubated at 4 °C for 5 h with gentle rotation. Bio-beads (0.3 g) were then added to remove detergents from the system and facilitate nanodisc formation. After incubation at 4 °C overnight, Bio-beads were removed through filtration, and protein-containing nanodiscs were collected for cryo-EM analysis after final purification by SEC in running buffer containing 25 mM Tris-HCl, pH 8.0, and 150 mM NaCl (Superose 6 Increase 10/300 GL, GE Healthcare).

### **Protein-drug sample preparation**

For rCa<sub>v</sub>1.1-1S reconstruction, (*S*)-(-)-Bay K8644 was added into the nanodisc reconstitution buffer at the final concentration of 1 µM. The mixture was purified by SEC in running buffer supplemented with 1 µM (*S*)-(-)-Bay K8644.



For rCa<sub>v</sub>1.1-10S/100S/100R/100A reconstructions, 10 μM, 100 μM (*S*)-(-)-Bay K8644, 100 μM (*R*)-(+)-Bay K8644 and 100 μM amlodipine was separately incubated with nanodisc-embedded proteins for 30 min before cryo-grids preparation.

### **Cryo-EM data acquisition**

Aliquots of 3.5 μl concentrated samples were loaded onto glow-discharged holey carbon grids (Quantifoil Cu R1.2/1.3, 300 mesh). Grids were blotted for 5 s and plunge-frozen in liquid ethane cooled by liquid nitrogen using a Vitrobot MarK IV (Thermo Fisher) at 8 °C with 100 percent humidity. Grids were transferred to a Titan Krios electron microscope (Thermo Fisher) operating at 300 kV and equipped with a Gatan Gif Quantum energy filter (slit width 20 eV) and spherical aberration (Cs) image corrector. Micrographs were recorded using a K2 Summit counting camera (Gatan Company) in super-resolution mode with a nominal magnification of 105,000x, resulting in a calibrated pixel size of 0.557 Å. Each stack of 32 frames was exposed for 5.6 s, with an exposure time of 0.175 s per frame. The total dose for each stack was ~ 50 e-/Å<sup>2</sup>. SerialEM was used for fully automated data collection (35). All 32 frames in each stack were aligned, summed, and dose weighted using MotionCorr2 and 2-fold binned to a pixel size of 1.114 Å/pixel (36-38). The defocus values were set from -1.9 to -2.1 μm and were estimated by Gctf (39).

### **Image processing**

Totals of 1739/2327/1595/1767/2092 cryo-EM micrographs were collected, and 644,294/714,871/560,063/621,407/686,403 particles were auto-picked by RELION-3.0 for rCa<sub>v</sub>1.1-100S, rCa<sub>v</sub>1.1-10S, rCa<sub>v</sub>1.1-1S, rCa<sub>v</sub>1.1-100R and rCa<sub>v</sub>1.1-100A in nanodiscs,

respectively (40). Particle picking was performed by RELION-3.0. All subsequent 2D and 3D classifications and refinements were performed using RELION-3.0. Reference-free 2D classification using RELION-3.0 was performed to remove ice spots, contaminants, and aggregates, yielding 581,802/701,745/463,685/537,339/506,092 particles, respectively. The particles were processed with a global search K=1 using RELION-3.0 to determine the initial orientation alignment parameters using bin2 particles. A published cryo-EM map of human rCa<sub>v</sub>1.1 was used as the initial reference. After 40 iterations, the datasets from the last 6 iterations were subject to local search 3D-classifications using 4 classes. Particles from good classes were then combined and re-extracted with a box size of 280 and binned pixel size of 1.114 Å for further refinement and 3D-classification, resulting in 157,294/207,038/135,210/146,737/184,373 particles, which were subjected to auto-refinement. 3D reconstructions were obtained at resolutions of 3.1 Å/3.5 Å/3.8 Å/3.4 Å/3.1 Å. Skip-alignment 3D classification using bin1 particles after Bayesian polish yielded data sets containing 87,516/53,789/53,341/94,696/184,373 particles respectively and resulted in respective reconstructions at 3.0 Å/3.4 Å/3.4 Å/3.2 Å/2.9 Å by using a core mask. Reported resolutions are based on the gold-standard Fourier shell correlation (FSC) 0.143 criterion. Before visualization, all density maps were corrected for the modulation transfer function of the detector and sharpened by applying a negative B-factor that was estimated using automated procedures. Local resolution variations were estimated using RELION 3.0.

### **Model building and refinement**

The previously reported model (PDB: 5JP5) was used as the starting model and docked into the rCa<sub>v</sub>1.1-100S, rCa<sub>v</sub>1.1-10S, rCa<sub>v</sub>1.1, rCa<sub>v</sub>1.1-100R and rCa<sub>v</sub>1.1-100A maps in Chimera (19). The

models were manually adjusted in COOT, followed by refinement against the corresponding maps by the phenix.real\_space\_refine program in PHENIX with secondary structure and geometry restraints. Statistics of 3D reconstruction and model refinement can be found in Table S1.

### **Competing interests**

No competing interests.

### **Data and materials availability**

Atomic coordinates and EM maps have been deposited in the PDB (<http://www.rcsb.org>) and EMDB (<https://www.ebi.ac.uk/pdbe/emdb>), respectively. For rCa<sub>v</sub>1.1 in complex with 100 μM, 10 μM (*S*)-(-)-Bay K8644, 1 μM (*S*)-(-)-Bay K8644 (apo in fact), 100 μM (*R*)-(+)-Bay K8644 and 100 μM amlodipine, the PDB codes are 7JPK, 7JPL, 7JPV, 7JPW, and 7JPX, respectively; EMDB codes are EMD- 22414, EMD- 22415, EMD- 22424, EMD- 22425, and EMD-22426, respectively.

### **Acknowledgments**

We thank the cryo-EM facility at Princeton Imaging and Analysis Center, which is partially supported by the Princeton Center for Complex Materials, a National Science Foundation (NSF)-MRSEC program (DMR-1420541). The work was supported by grant from NIH (5R01GM130762).

## References:

1. W. A. Catterall, Voltage-gated calcium channels. *Cold Spring Harb Perspect Biol* **3**, a003947 (2011).
2. D. E. Clapham, Calcium signaling. *Cell* **131**, 1047-1058 (2007).
3. E. A. Ertel *et al.*, Nomenclature of voltage-gated calcium channels. *Neuron* **25**, 533-535 (2000).
4. M. C. Nowycky, A. P. Fox, R. W. Tsien, Three types of neuronal calcium channel with different calcium agonist sensitivity. *Nature* **316**, 440-443 (1985).
5. G. W. Zamponi, J. Striessnig, A. Koschak, A. C. Dolphin, The Physiology, Pathology, and Pharmacology of Voltage-Gated Calcium Channels and Their Future Therapeutic Potential. *Pharmacol Rev* **67**, 821-870 (2015).
6. G. W. Zamponi, Targeting voltage-gated calcium channels in neurological and psychiatric diseases. *Nat Rev Drug Discov* **15**, 19-34 (2016).
7. E. M. Sorkin, S. P. Clissold, R. N. Brogden, Nifedipine. A review of its pharmacodynamic and pharmacokinetic properties, and therapeutic efficacy, in ischaemic heart disease, hypertension and related cardiovascular disorders. *Drugs* **30**, 182-274 (1985).
8. A. C. Dolphin, A short history of voltage-gated calcium channels. *Br J Pharmacol* **147** Suppl 1, S56-62 (2006).
9. G. H. Hockerman, B. Z. Peterson, B. D. Johnson, W. A. Catterall, Molecular determinants of drug binding and action on L-type calcium channels. *Annu Rev Pharmacol Toxicol* **37**, 361-396 (1997).
10. S. Goldmann, J. Stoltefuss, 1, 4-Dihydropyridines: effects of chirality and conformation on the calcium antagonist and calcium agonist activities. *Angewandte Chemie International Edition in English* **30**, 1559-1578 (1991).
11. G. Franckowiak, M. Bechem, M. Schramm, G. Thomas, The optical isomers of the 1, 4-dihydropyridine BAY K 8644 show opposite effects on Ca channels. *European journal of pharmacology* **114**, 223-226 (1985).
12. M. Schramm, G. Thomas, R. Towart, G. Franckowiak, Novel dihydropyridines with positive inotropic action through activation of Ca<sup>2+</sup> channels. *Nature* **303**, 535-537 (1983).
13. G. P. Dubé, Y. H. Baik, A. Schwartz, Effects of a novel calcium channel agonist dihydropyridine analogue, Bay k 8644, on pig coronary artery: biphasic mechanical response and paradoxical potentiation of contraction by diltiazem and nimodipine. *Journal of cardiovascular pharmacology* **7**, 377-389 (1985).
14. M. Bechem, H. Hoffmann, The molecular mode of action of the Ca agonist (–) BAY K 8644 on the cardiac Ca channel. *Pflügers Archiv* **424**, 343-353 (1993).
15. J. M. Monti, M. Hawkins, H. Jantos, L. D'Angelo, M. Fernández, Biphasic effects of dopamine D-2 receptor agonists on sleep and wakefulness in the rat. *Psychopharmacology* **95**, 395-400 (1988).
16. A. A. Rey, M. Purrio, M.-P. Viveros, B. Lutz, Biphasic effects of cannabinoids in anxiety responses: CB1 and GABA B receptors in the balance of GABAergic and glutamatergic neurotransmission. *Neuropsychopharmacology* **37**, 2624-2634 (2012).
17. J. Wu *et al.*, Structure of the voltage-gated calcium channel Cav1. 1 complex. *Science* **350**, aad2395 (2015).

18. J. Wu *et al.*, Structure of the voltage-gated calcium channel Ca<sub>v</sub>1.1 at 3.6 Å resolution. *Nature* **537**, 191-196 (2016).
19. Y. Zhao *et al.*, Molecular basis for ligand modulation of a mammalian voltage-gated Ca<sub>2+</sub> channel. *Cell* **177**, 1495-1506. e1412 (2019).
20. Y. Zhao *et al.*, Cryo-EM structures of apo and antagonist-bound human Cav3.1. *Nature* **576**, 492-497 (2019).
21. S. Gao *et al.*, Employing NaChBac for cryo-EM analysis of toxin action on voltage-gated Na<sup>+</sup> channels in nanodisc. *Proceedings of the National Academy of Sciences*, (2020).
22. B. Z. Peterson, T. N. Tanada, W. A. Catterall, Molecular determinants of high affinity dihydropyridine binding in L-type calcium channels. *Journal of Biological Chemistry* **271**, 5293-5296 (1996).
23. R. S. Kass, J. P. Arena, Influence of Ph0 on Calcium-Channel Block by Amlodipine, a Charged Dihydropyridine Compound - Implications for Location of the Dihydropyridine Receptor. *J Gen Physiol* **93**, 1109-1127 (1989).
24. J. E. Arrowsmith *et al.*, Long-Acting Dihydropyridine Calcium-Antagonists .1. 2-Alkoxyethyl Derivatives Incorporating Basic Substituents. *J Med Chem* **29**, 1696-1702 (1986).
25. H. Shen *et al.*, Structure of a eukaryotic voltage-gated sodium channel at near-atomic resolution. *Science (New York, N.Y)* **355**, (2017).
26. Z. Yan *et al.*, Structure of the Nav1.4-beta1 Complex from Electric Eel. *Cell* **170**, 470-482 e411 (2017).
27. H. Shen *et al.*, Structural basis for the modulation of voltage-gated sodium channels by animal toxins. *Science*, (2018).
28. X. Pan *et al.*, Structure of the human voltage-gated sodium channel Nav1.4 in complex with beta1. *Science (New York, N.Y)* **362**, (2018).
29. X. Pan *et al.*, Molecular basis for pore blockade of human Na<sup>(+)</sup> channel Nav1.2 by the mu-conotoxin KIIIA. *Science* **363**, 1309-1313 (2019).
30. H. Shen, D. Liu, K. Wu, J. Lei, N. Yan, Structures of human Nav1.7 channel in complex with auxiliary subunits and animal toxins. *Science (New York, N.Y)* **363**, 1303-1308 (2019).
31. S. Gao *et al.*, Employing NaChBac for cryo-EM analysis of toxin action on voltage-gated Na<sup>(+)</sup> channels in nanodisc. *Proc Natl Acad Sci U S A* **117**, 14187-14193 (2020).
32. H. Affolter, R. Coronado, Agonists Bay-K8644 and Cgp-28392 Open Calcium Channels Reconstituted from Skeletal-Muscle Transverse Tubules. *Biophys J* **48**, 341-347 (1985).
33. M. Bechem, M. Schramm, Calcium-Agonists. *J Mol Cell Cardiol* **19**, 63-75 (1987).
34. A. M. Brown, D. L. Kunze, A. Yatani, The Agonist Effect of Dihydropyridines on Ca-Channels. *Nature* **311**, 570-572 (1984).
35. J. Lei, J. Frank, Automated acquisition of cryo-electron micrographs for single particle reconstruction on an FEI Tecnai electron microscope. *Journal of structural biology* **150**, 69-80 (2005).
36. S. Q. Zheng *et al.*, MotionCor2: anisotropic correction of beam-induced motion for improved cryo-electron microscopy. *Nature methods* **14**, 331-332 (2017).
37. T. Grant, N. Grigorieff, Measuring the optimal exposure for single particle cryo-EM using a 2.6 Å reconstruction of rotavirus VP6. *Elife* **4**, e06980 (2015).
38. X. Li *et al.*, Electron counting and beam-induced motion correction enable near-atomic-resolution single-particle cryo-EM. *Nature methods* **10**, 584 (2013).

39. K. Zhang, Gctf: Real-time CTF determination and correction. *Journal of structural biology* **193**, 1-12 (2016).
40. S. H. Scheres, RELION: implementation of a Bayesian approach to cryo-EM structure determination. *Journal of structural biology* **180**, 519-530 (2012).

**Figure 1**

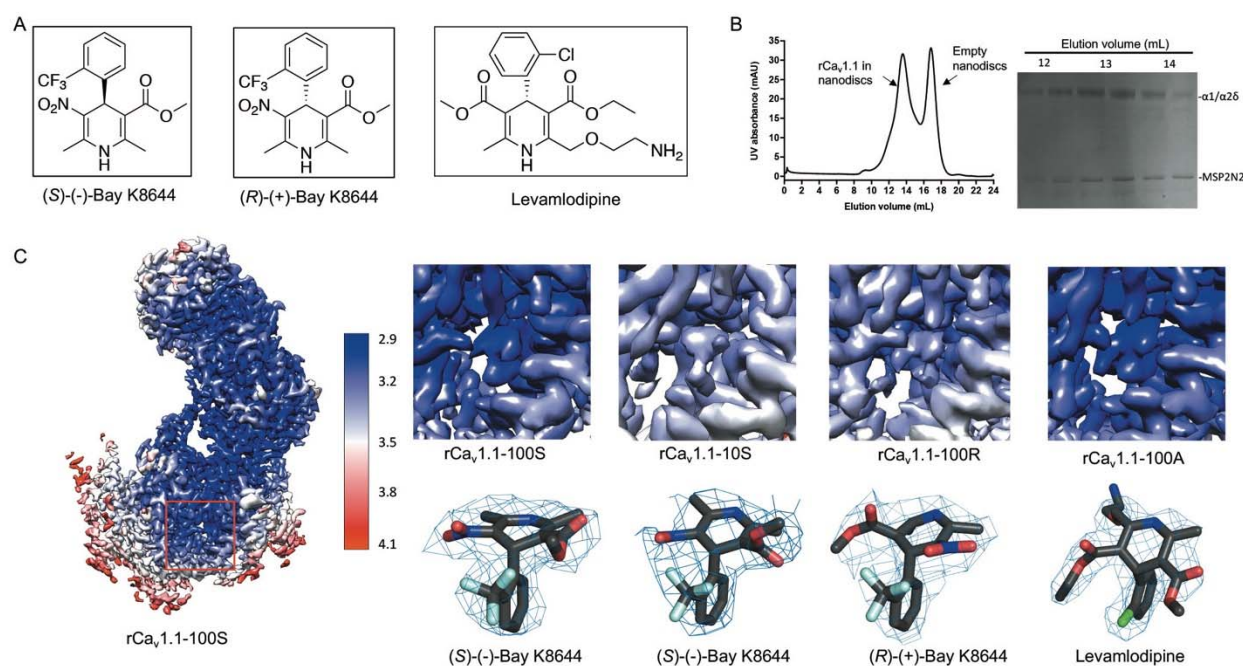




**Figure 2**

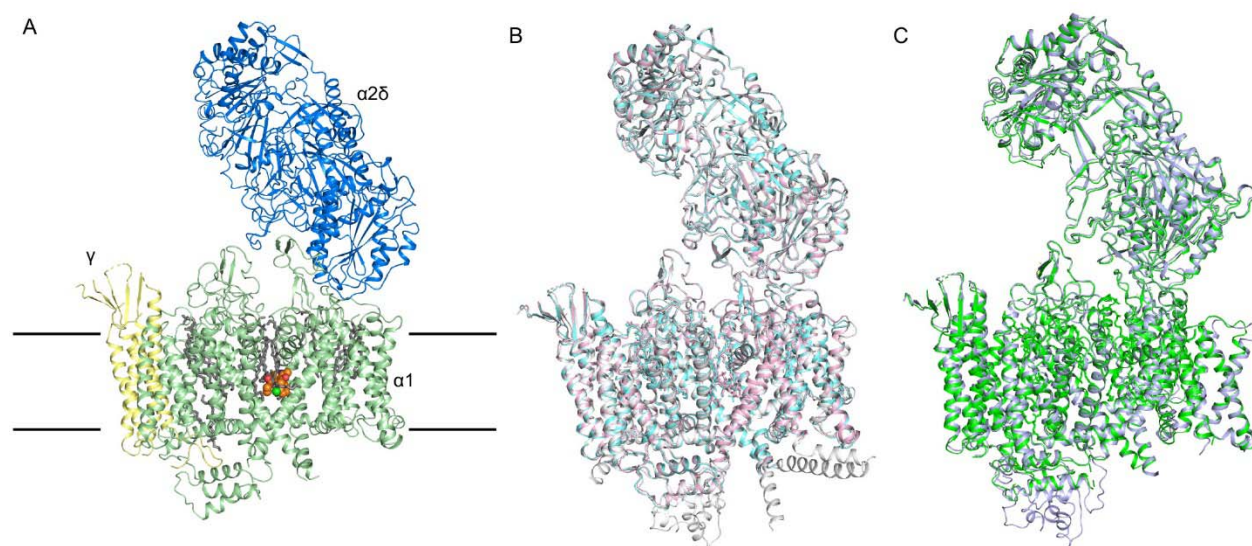




**Figure 3**

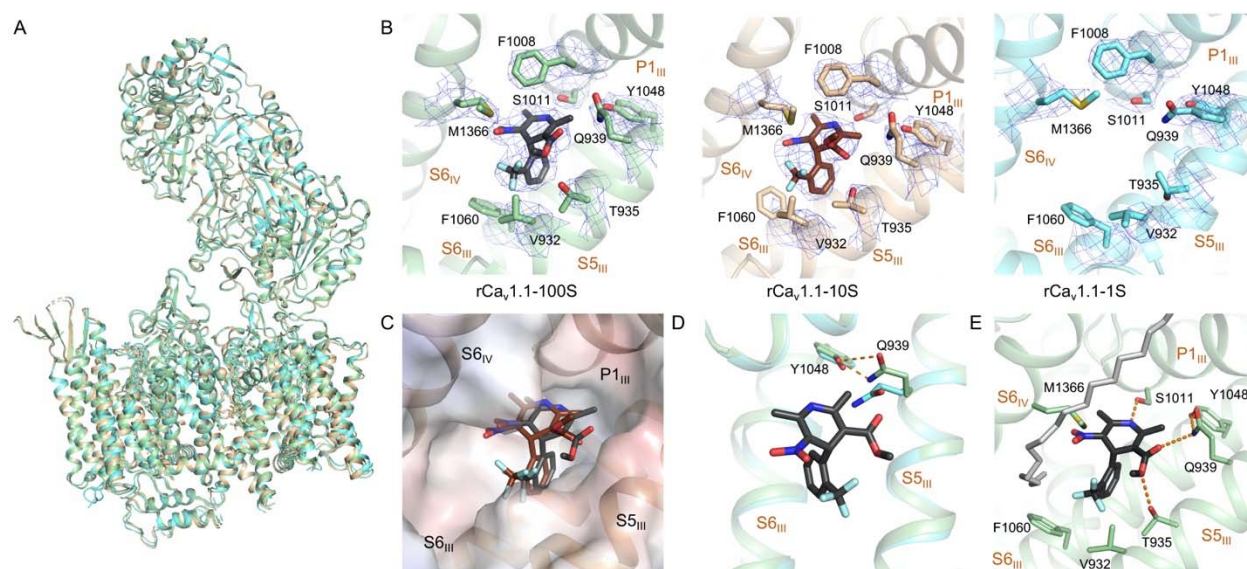


**Figure 4**

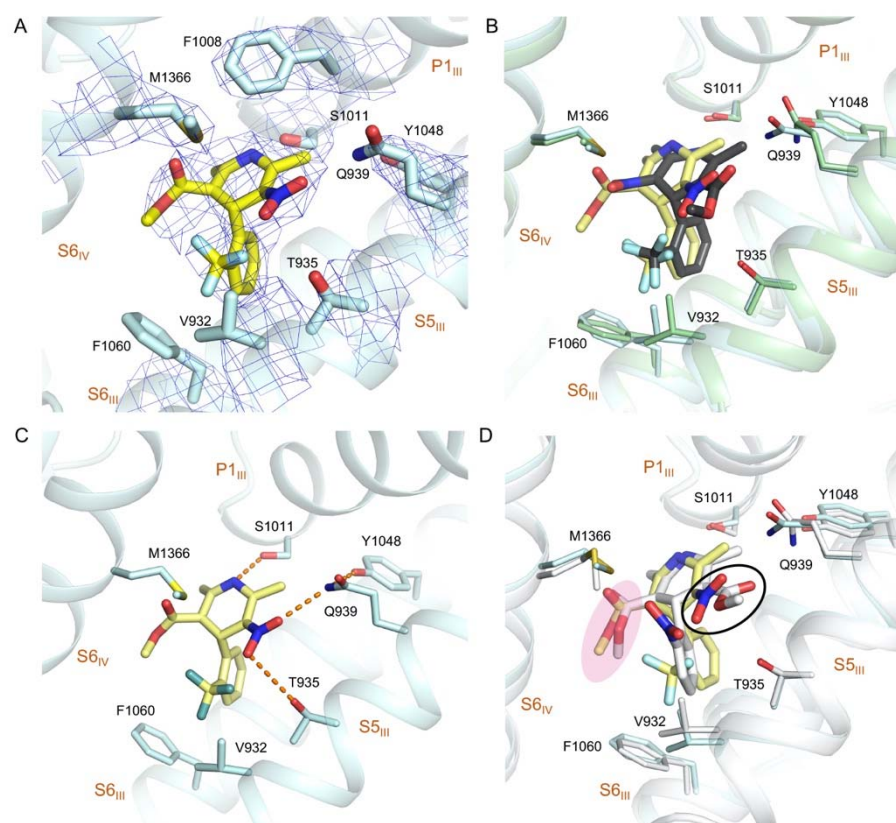


**Figure 5**

